Inflammatory response in hematopoietic stem and progenitor cells triggered by activating SHP2 mutations potentiates leukemogenesis

Maja Solman[1], Sasja Blokzijl-Franke[1,*], Florian Piques[2,3,*], Chuan Yan[4,5,6,7], Qiqi Yang[4,5,6,7], Marion Strullu[2,8], Sarah M. Kamel[1], Pakize Ak[1], Jeroen Bakkers[1,9], David M. Langenau[4,5,6,7], Hélène Cavé[2,3], Jeroen den Hertog[1,10,#]

[1] Hubrecht Institute-KNAW and UMC Utrecht, 3584 CT Utrecht, the Netherlands

[2] INSERM UMR_S1131, Institut de Recherche Saint-Louis, University of Paris, Paris, France

[3] Assistance Publique des Hôpitaux de Paris AP-HP, Hôpital Robert Debré, Département de Génétique, Paris, France

[4] Molecular Pathology Unit, Massachusetts General Hospital Research Institute, Charlestown, MA 02129, United States of America

[5] Massachusetts General Hospital Cancer Center, Charlestown, MA 02129, United States of America

[6] Center for Regenerative Medicine, Massachusetts General Hospital, Boston, MA 02114, United States of America

[7] Harvard Stem Cell Institute, Cambridge, MA 02139, United States of America

[8] Assistance Publique des Hôpitaux de Paris AP-HP, Hôpital Robert Debré, Service d'Onco-Hématologie Pédiatrique, Paris, France

[9]Department of Medical Physiology, Division of Heart and Lungs, UMC Utrecht, 3584 CX Utrecht, the Netherlands

[10] Institute of Biology Leiden, Leiden University, 2333 BE Leiden, The Netherlands

* These authors contributed equally

Jeroen den Hertog, **Address**: Hubrecht Institute-KNAW and UMC Utrecht, 3584 CT Utrecht, the Netherlands, **Telephone**: +31 30 212 1800, **Email:** j.denhertog@hubrecht.eu

Abstract

Activating mutations in the protein-tyrosine phosphatase SHP2 are the most frequently occurring mutations in juvenile myelomonocytic leukemia (JMML) and JMML-like myeloproliferative neoplasm (MPN) associated with Noonan syndrome (NS). Hematopoietic stem and progenitor cells (HSPCs) are the disease propagating cells of JMML. Here, we explored transcriptomes of HSPCs with Shp2 mutations derived from JMML patients and a novel NS zebrafish model. In addition to major NS traits, CRISPR/Cas9 knock-in Shp2^{D61G} mutant zebrafish recapitulated a JMML-like MPN phenotype, including myeloid lineage hyperproliferation, *ex vivo* growth of myeloid colonies and *in vivo* transplantability of HSPCs. Single cell mRNA sequencing of HSPCs from Shp2^{D61G} zebrafish embryos and bulk sequencing of HSPCs from JMML patients revealed an overlapping inflammatory gene expression pattern. Strikingly, an anti-inflammatory agent rescued JMML-like MPN in Shp2^{D61G} zebrafish embryos. Our results indicate that a common inflammatory response was triggered in the HSPCs from sporadic JMML patients and syndromic NS zebrafish, which potentiated MPN and may represent a future target for JMML therapies.

Introduction

A broad spectrum of germline activating mutations in the tyrosine phosphatase SHP2, encoded by *PTPN11* has been found to cause Noonan syndrome (NS), a dominantly inherited developmental disorder from the RASopathy group affecting 1:1,500 individuals. NS is characterized by a systemic impact on development, most commonly resulting in short stature, congenital heart defects and specific craniofacial characteristics (Rauen, 2013; Tajan et al., 2018). Somatic activating mutations in *PTPN11* are the most common cause of sporadic juvenile myelomonocytic leukemia (JMML), a rare but aggressive myelodysplastic and myeloproliferative neoplasm (MPN) occurring in young children (Caye et al., 2015; Tartaglia et al., 2003). Consistently, children with NS are predisposed to developing neonatal MPN, that either regress without treatment or rapidly progress to JMML leading to early death (Kratz et al., 2005; Strullu et al., 2014). Previous studies support the view of a strong endogenous role of germline *PTPN11* mutations in the occurrence of myeloproliferative complications with the existence of high-risk mutations (Mulero-Navarro et al., 2015; Strullu et al., 2014). Given the aggressive nature of JMML and lack of therapies, a better understanding of the elusive JMML(-like MPN) pathophysiology and development of reliable preclinical models are essential.

Several lines of evidence indicate the importance of prenatal hematopoiesis such as the young age window for both NS-associated and sporadic JMML. The prenatal origin of *PTPN11* mutations in sporadic JMML suggests that JMML and NS-associated JMML-like MPN originate from fetal hematopoiesis (Behnert et al., 2021). Studying SHP2-driven JMML(-like MPN) during fetal hematopoiesis is challenging in conditional knock-in mouse models of JMML with *PTPN11* mutations, because mutant SHP2 expression is induced only postnatally (Chan et al., 2009; Xu et al., 2011) or indolent MPN is induced (Tarnawsky et al., 2017, 2018). NS knock-in mice with activating *PTPN11* mutations develop mild MPN only after 5 months of age (Araki et al., 2004, 2009).

Zebrafish (*Danio rerio*) with rapid *ex-utero* development, transparent embryos and conserved blood ontogeny emerged as a unique pediatric leukemia model that enables monitoring of leukemogenesis from its initial stages with high temporal and spatial resolution (de Pater & Trompouki, 2018; Gore et al., 2018). Furthermore, NS-associated features, such as shorter body axis length, craniofacial defects, defective

gastrulation and impaired heart looping, are recapitulated in zebrafish embryos upon transient over-expression of NS-associated protein variants (Bonetti et al., 2014; Jopling et al., 2007; Niihori et al., 2019; Paardekooper Overman et al., 2014; Runtuwene et al., 2011).

To better assess the link between dysregulated SHP2 and myeloproliferation in the context of NS, we developed and characterized a novel genetic zebrafish model of NS with Shp2-D61G mutation, an NS-associated mutation that is most frequently associated with NS/JMML-like MPN in human patients (Strullu et al., 2014; Tartaglia et al., 2001). Mutant zebrafish developed hematopoietic defects consistent with JMML-like MPN. Transcriptomic comparison of HSPCs obtained from JMML patients with somatic *PTPN11* mutations and HSPCs from mutant zebrafish harboring an NS-associated variant of Shp2, suggested common mechanisms of disease initiation in sporadic and syndromic PTPN11-driven JMML. Both data sets show a similar pro-inflammatory gene expression and an anti-inflammatory agent largely rescued the hematopoietic defects in mutant zebrafish, suggesting inflammation as potential drug target for sporadic and syndromic JMML(-like MPN). Our data show that Shp2-mutant zebrafish convincingly model the human NS-associated MPN thereby providing a valuable preclinical model for development of future therapies.

Results

Shp2^{D61G} mutant zebrafish display typical Noonan syndrome traits

To investigate early hematopoietic defects associated with NS in a vertebrate animal model, we turned to zebrafish, which represents a versatile model to study leukemogenesis and in which it is feasible to introduce mutations at will using CRISPR/Cas9-mediated homology directed repair (Tessadori et al., 2018). Certain NS mutations are more frequently associated with NS/JMML-like MPN than others. The D61G substitution in SHP2 is the most frequently occurring (Strullu et al., 2014; Tartaglia et al., 2001). Thus, we introduced the D61G mutation in zebrafish Shp2a using CRISPR/Cas9-mediated homology directed repair (**Supplementary Fig. 1a**), targeting the *ptpn11a* gene. Sequencing confirmed that the oligonucleotide used for the homology directed repair was incorporated correctly into the genome (**Fig. 1a**) and that the introduced mutation did not have a detectable effect on Shp2a protein expression (**Fig. 1b**). Prior to phenotypic analyses, the mutant lines were outcrossed twice to ensure that potential background mutations due to the CRISPR/Cas9 approach were removed.

In 32% of Shp2$^{D61G/wt}$ and 45% of Shp2$^{D61G/D61G}$ embryos at 5 days post fertilization (dpf) we observed typical Noonan syndrome traits, such as reduced body axis extension, heart edema and face deformities. Based on the extent of the phenotypes, defects were categorized as normal, mild and severe. (**Fig. 1c,d**). The observed phenotypic defects were mostly mild, but in some cases severe defects were found, including severely stunted growth, edemas of the heart and jaw, and absence of the swim bladder (**Fig. 1c,d**). A more detailed characterization of the typical NS traits showed that the body axis length was significantly reduced in Shp2^{D61G} mutant embryos at 5dpf (**Fig. 1e**). Furthermore, imaging of Alcian blue stained cartilage revealed NS-reminiscent craniofacial defects in 4dpf Shp2^{D61G} mutant embryos, characterized by broadening of the head (**Fig. 1f**), leading to an increased ratio of the width of the ceratohyal and the distance to Meckel's cartilage (**Fig. 1g**). We also assessed the general morphology and function of the mutant embryonic hearts. Whole-mount *in situ* hybridization (WISH) with cardiomyocyte (*myl7*), ventricular (*vhmc*) and atrial (*ahmc*) markers identified no obvious morphological heart defects, such as changes in heart size or heart looping, as well as heart chamber specification at 3dpf (**Supplementary Fig. 1b**). A decrease in

heart rate (**Fig. 1i)**, ejection fraction and cardiac output (**Supplementary Fig. 1c,d**) was detected from the ventricular kymographs obtained from high speed video recordings (Tessadori et al., 2012) of the Shp2^{D61G} mutant hearts at 5dpf **(Fig. 1h**). Effects on cardiac function varied from embryo to embryo, which is reminiscent of variable heart defects in human patients.

Since most of the embryos with obvious phenotypic defects did not develop a swim bladder, they did not survive to adulthood. The rest of both Shp2$^{D61G/wt}$ and Shp2$^{D61G/D61G}$ mutant zebrafish grew up normally and displayed rather mild defects in adult stages, such as shorter body axis (**Fig. 1j**), with markedly reduced length observed from the embryonic stage of 5dpf until the fully developed adults (**Fig. 1k**). In 10% of Shp2^{D61G} mutants the phenotypes were more severe, with markedly reduced body axis length compared to their siblings, skinny appearance and with overall redness, especially in the head and gill region (**Fig. 1j**).

Taken together, the NS Shp2^{D61G} mutant zebrafish we established phenocopied several of the typical NS traits, such as stunted growth, craniofacial defects, and heart defects. Similar to differences in symptoms observed in individual human patients, the severity of the defects varied among individual Shp2^{D61G} mutant zebrafish.

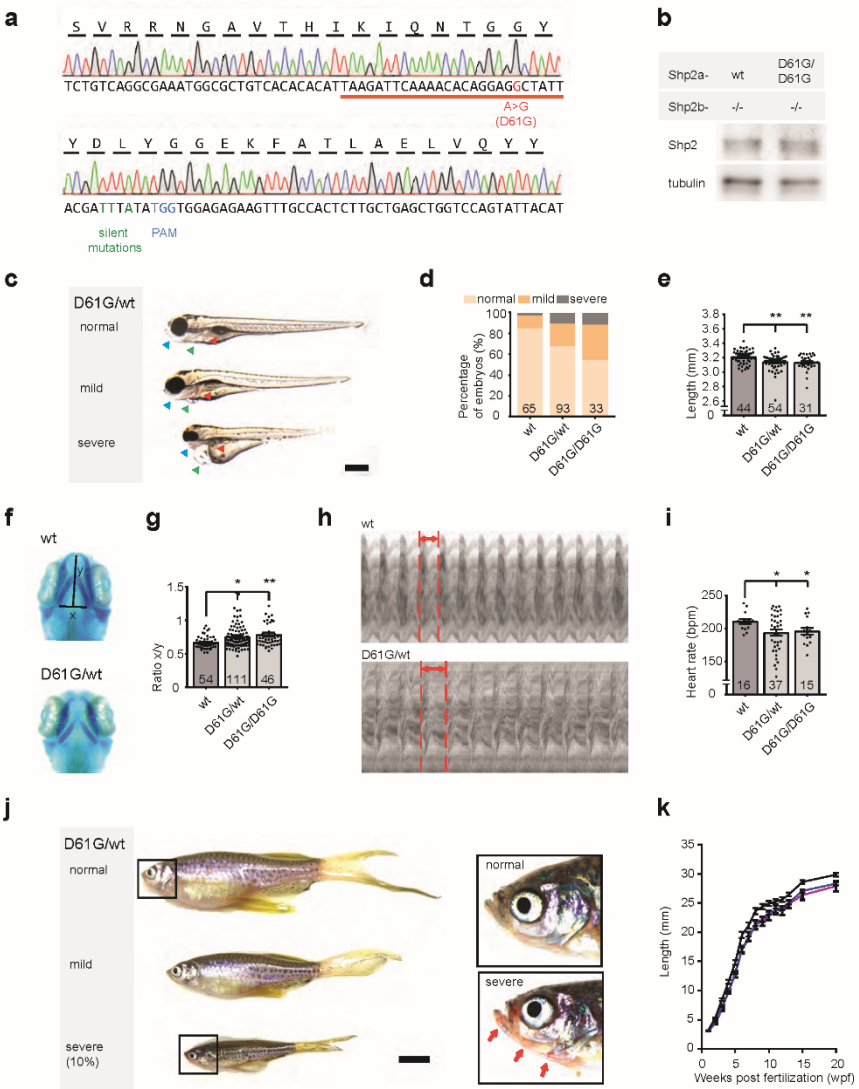

Figure 1. Shp2^{D61G} zebrafish display NS-like traits. a Sequencing trace derived from Shp2$^{D61G/D61G}$ zebrafish. Oligonucleotide sequence used to generate the model is underlined. Nucleotide substitutions for D61G mutation (red), silent mutations close to the PAM site (green) and the PAM site (blue) are indicated. **b** Immunoblot of Shp2 levels from 5 pooled Shp2a^{wt}Shp2b$^{-/-}$ or Shp2a$^{D61G/D61G}$Shp2b$^{-/-}$ embryos using antibodies for Shp2 and tubulin (loading control). **c** Representative images of typical Shp2^{D61G} zebrafish embryonic phenotypes at 5dpf. Blue arrows: jaw, green arrows: heart, red arrows: swim bladder. **d** Quantification of phenotypes of Shp2^{wt}, Shp2$^{D61G/wt}$ and Shp2$^{D61G/D61G}$ embryos scored as in **c** normal, mild and severe. **e** Body axis length of Shp2^{wt}, Shp2$^{D61G/wt}$ and Shp2$^{D61G/D61G}$ embryos at 5dpf. **f** Representative images of Alcian blue stained head-cartilage of 4dpf Shp2^{wt} and Shp2$^{D61G/wt}$ embryos. (x) width of ceratohyal, (y) distance to Meckel's cartilage. **g** Quantified craniofacial defects (x/y ratio). **h** Representative ventricular kymographs derived from high speed video recordings of beating hearts of 5dpf Shp2^{wt} and Shp2$^{D61G/wt}$ embryos. Red dotted lines indicate one heart period. **i** Heart rates derived from the ventricular kymographs. **j** Representative images of typical Shp2^{D61G} zebrafish adult phenotypes at 24wpf. Red arrows indicate skin redness in the jaw region. Scale bar is 0.5cm. Insets, zoom-in of boxed regions. **k** Body axis lengths of 10 Shp2^{wt}, 25 Shp2$^{D61G/wt}$ and 10 Shp2$^{D61G/D61G}$ zebrafish measured weekly between 5dpf and 20wpf of age. **d,e,g,i** Measurements originate from three distinct experiments. Number on bars: number of embryos. **e,g,i,k** Error bars: standard error of the mean (SEM), *p < 0.05; **p < 0.01, ANOVA complemented by Tukey HSD.

Shp2^{D61G} zebrafish embryos develop myeloproliferative blood defect originating in defective HSPCs

Next we explored hematopoietic abnormalities in the Shp2^{D61G} zebrafish during embryonic development, corresponding to prenatal hematopoietic ontogeny in human. We were not able to observe any effect of the Shp2^{D61G} mutation on primitive hematopoiesis in embryos at 2dpf using WISH for markers of erythroid progenitors (*gata-1*), myeloid progenitors (*pu.1*) and white blood cells (*l-plastin*) (**Supplementary Fig. 2a**). On the other hand, a significant effect of the Shp2-D61G mutation on definitive hematopoiesis was observed at 5dpf (**Fig. 2**). An increased number of HSPCs marked by CD41-GFP^{low} was observed in the caudal hematopoietic tissue region (CHT, corresponding to the fetal liver in human) and the head kidney (corresponding to the bone marrow in human) of the mutant embryos **(Fig. 2a,b)**. Shp2^{D61G} mutation seems to affect both proliferation and apoptosis of HSPCs, evident by an increase in CD41-GFP^{low} cells positive for phosphohistone H3 (pHis3), a marker for late G2 and M phase and a decrease in Acridine orange positive cells in the CHT region, marking apoptotic cells (**Supplementary Fig. 2b,c**). We observed an increase of *c-myb* positive cells, marking HSPCs and of *l-plastin* positive cells, marking all white blood cells, in both CHT and head kidney region of the Shp2^{D61G} mutants (**Fig. 2c-f**). These latter cells appear not to be lymphocytes, since the size of the *ikaros*-positive thymus, was not affected (**Supplementary Fig. 2d,e**). On the other hand, the myeloid lineage was markedly expanded, evident from the increase in the number of mpx-GFP positive neutrophils (**Fig. 2g,h**), and mpeg-mCherry positive macrophages (**Fig. 2g,i**), in the Tg(*mpx:GFP, mpeg:mCherry*) double transgenic mutant embryos. Shp2^{D61G} mutant embryos also displayed a mild decrease in the number of thrombocytes, marked by CD41-GFP^{high} in the Tg(*cd41:GFP, kdrl:mCherry-CAAX*) transgenic line, and number of *β-globin* positive erythrocytes (**Supplementary Fig. 2f-h)**. The observed defects in all different blood lineages examined here were stronger in the homozygous Shp2$^{D61G/D61G}$ than heterozygous Shp2$^{D61G/wt}$ embryos, supporting a dosage effect. One of the clinical hallmarks of JMML is the hypersensitivity of myeloid progenitors to GM-CSF. In zebrafish, effects of stimulation by Gcsfa or Gscfb corresponds to the GM-CSF stimulation in human (Svoboda et al., 2016). Compared to their wt siblings, colonies developed from the CD41-GFP^{high} cells isolated from the Shp2^{D61G} zebrafish

embryos at 5dpf and exposed to Gcsfa were larger in size and number, demonstrating an enhanced GM colony forming ability (**Fig. 2j,k)**. Finally, we tested whether the observed myeloid expansion was reconstituted upon transplantation of the WKM cells harvested from Shp2$^{D61G/wt}$ animals in the Tg(*mpx:GFP, mpeg:mCherry*) background into the optically clear recipient *prkdc-/-* immunodeficient zebrafish (Moore et al., 2016). Animals injected with 1x10^5 mutant WKM cells (3/5) accumulated GFP- and mCherry- positive cells near the site of injection starting at 14 days and increasing until 28 days. By contrast, animals injected with WKM cells from control sibling animals with wt Shp2a (5/5) lacked any GFP- and mCherry- positive cells (**Fig. 2l**).

Our findings suggest that the Shp2^{D61G} mutant zebrafish embryos develop multilineage hematopoietic defects during the definitive wave of fetal hematopoiesis, which originates in the HSPCs compartment. The observed defect is reminiscent of JMML-like MPN in human NS patients.

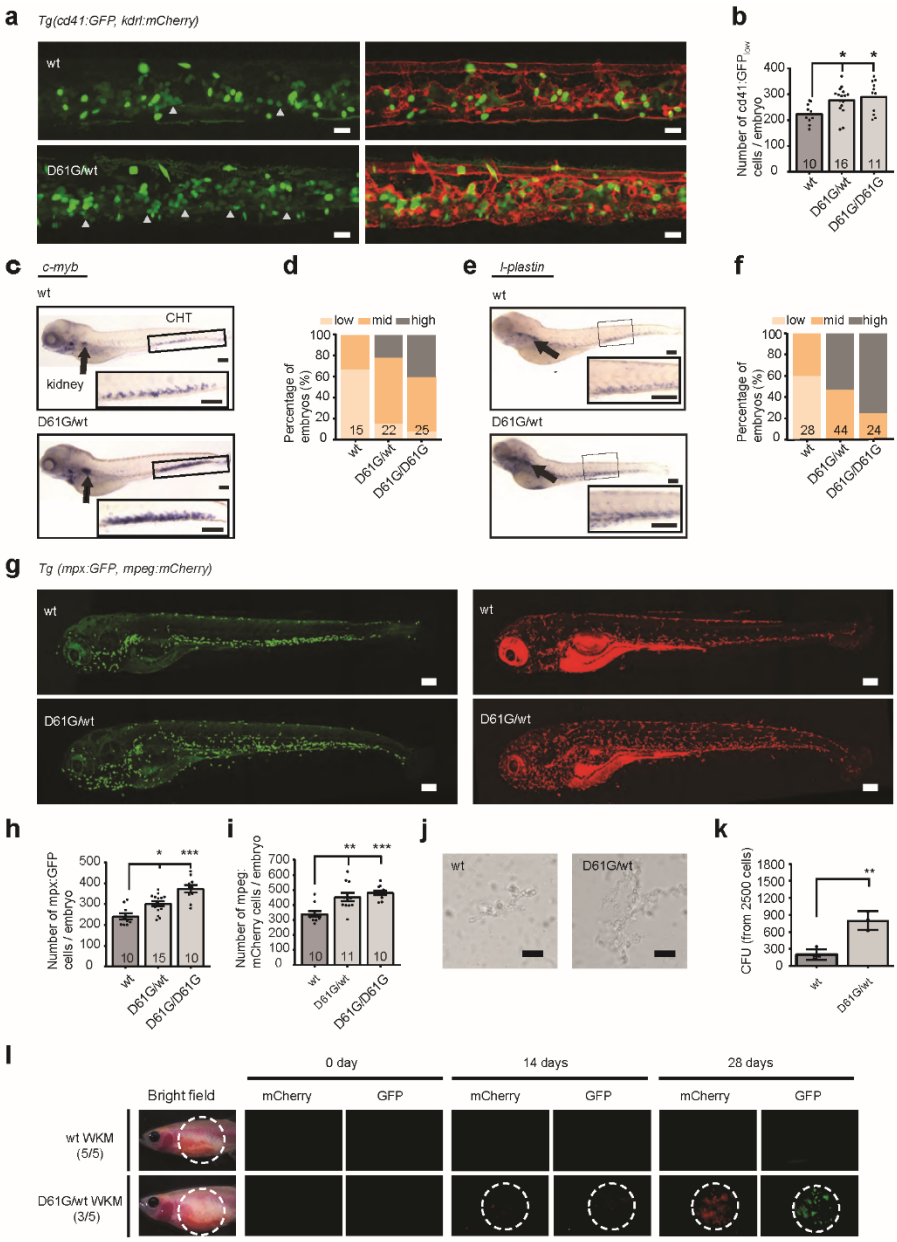

Figure 2. Shp2^{D61G} mutant zebrafish embryos display JMML-like MPN. a Representative images of the CHT region of Shp2^{wt} and Shp2^{D61G} zebrafish embryos in Tg(*cd41:GFP, kdrl:mCherry-CAAX*) background at 5dpf. *cd41:GFP^{low}* cells mark HSPCs and *cd41:GFP^{high}* cells thrombocytes. Grey arrow heads indicate *cd41:GFP^{low}* cells. Scale bar, 20µm. **b** The low intensity *cd41:GFP* positive cells in the CHT region were counted. **c** WISH of 5dpf Shp2^{wt} and Shp2$^{D61G/wt}$ embryos using *c-myb* specific probe. Head kidney (arrow) and CHT (box) are indicated; zoom-in in insert. Scale bars, 150µm. **d** Quantification of *c-myb* WISH. *C-myb* expression in Shp2^{wt}, Shp2$^{D61G/wt}$ and Shp2$^{D61G/D61G}$ embryos was scored as low, mid and high. **e** WISH of 5dpf Shp2^{wt} and Shp2$^{D61G/wt}$ embryos using *l-plastin* specific probe. Head kidney (arrow) and CHT (box) are indicated and zoom-in in insert. Scale bars,150µm. **f** Quantification of *l-plastin* expression in Shp2^{wt}, Shp2$^{D61G/wt}$ and Shp2$^{D61G/D61G}$ embryos scored as low, mid and high. **g** Representative images of Shp2^{wt} and Shp2^{D61G} zebrafish embryos in Tg(*mpx:GFP, mpeg:mCherry*) background at 5dpf. *Mpx*:GFP marks neutrophils and *mpeg*:mCherry macrophages. Scale bars,150µm. **h,i** Number of *mpx*:GFP and *mpeg*:mCherry positive cells per embryo. **j** Representative images of colonies developed from *cd41:GFP^{low}* cells isolated from the CHT of 5dpf Shp2^{wt} and Shp2$^{D61G/wt}$ zebrafish embryos, grown in methylcellulose with zebrafish cytokine Gcsfa for 2 days. Scale bar, 50µm. **k** Quantification of number of colonies from **j**, t-test. **l** WKM cells harvested from Shp2^{wt} and Shp2^{D61G} zebrafish in the Tg(*mpx:GFP, mpeg:mCherry*) background were injected into the peritoneum of adult *prkdc*-/- zebrafish. Recipients were monitored by fluorescence imaging. **b,d,f,h,i,k** Measurements originate from at least three distinct experiments. Number on bars: number of embryos. **b,h,i,k** Error bars represent SEM. *p < 0.05, **p<0.01, ***p<0.001. **b,h,i** ANOVA complemented by Tukey HSD.

Myeloid bias is established during early differentiation of Shp2^{D61G} HSPCs

In an effort to better understand the pathogenesis mechanisms in the Shp2^{D61G} mutant HSPCs, single cell RNA sequencing was performed using SORT-Seq on CD41-GFP^{low} cells derived from 5dpf Shp2^{wt}, Shp2$^{D61G/wt}$ and Shp2$^{D61G/D61G}$ zebrafish embryos in the Tg(*cd41*:*GFP*, *kdrl*:*mCherry-CAAX*) transgenic background (**Fig. 3a,b**). To group cells based on their transcriptional program, unsupervised clustering was performed using the RaceID3 package (Herman et al., 2018). Clusters were visualized by *t*-distributed stochastic neighbor embedding (*t*-SNE) and 4 major clusters were further analyzed (**Fig. 3c)**. Based on the differentially expressed genes and GO term analysis, cells from Cluster 1 were determined to be thrombocyte and erythroid progenitors, Cluster 2 HSC-like HSPCs, Cluster 3 early myeloid progenitors and Cluster 4 monocyte/macrophage progenitors (**Fig. 3c, Supplementary Fig. 3a, Supplementary Table 1**). A small subset of cells in Cluster 4 represented more differentiated neutrophils (**Supplementary Fig. 3b**).

HSPCs of either Shp2^{wt} or mutant Shp2$^{D61G/wt}$ and Shp2$^{D61G/D61G}$ genotypes were present in all 4 major clusters, indicating that distinct HSPCs phenotypes were maintained on a gene transcription level. However, the distribution of cells in clusters differed among genotypes. An overrepresentation of mutant Shp2$^{D61G/wt}$ and Shp2$^{D61G/D61G}$ cells was observed in the HSC-like HSPCs cluster and monocytes/macrophages progenitors cluster, whereas these were underrepresented in the thrombocyte and erythroid progenitors cluster **(Fig. 3d,e**). To validate this observation, we investigated the expression of *pu.1* and *alas2* markers in Shp2^{D61G} embryos of different genotypes by WISH. In the single cell RNA sequencing dataset, expression of *pu.1* and *alas2* was upregulated in the myeloid progenitors and erythroid progenitors, respectively (**Fig. 3f,i**). An increased number of *pu.1* positive cells was detected by WISH in 5dpf old Shp2^{D61G} embryos compared to their Shp2^{wt} siblings (**Fig. 3g,h**), whereas the number of *alas2* positive cells in Shp2^{D61G} mutants was decreased (**Fig. 3j,k**).

Taken together, single cell RNA sequencing suggests that defects during early differentiation of HSPCs to monocyte/macrophage progenitors and erythroid/thrombocyte progenitors initiate the multilineage blood defect observed in Shp2^{D61G} embryos, which recapitulates features of NS-JMML-like MPN.

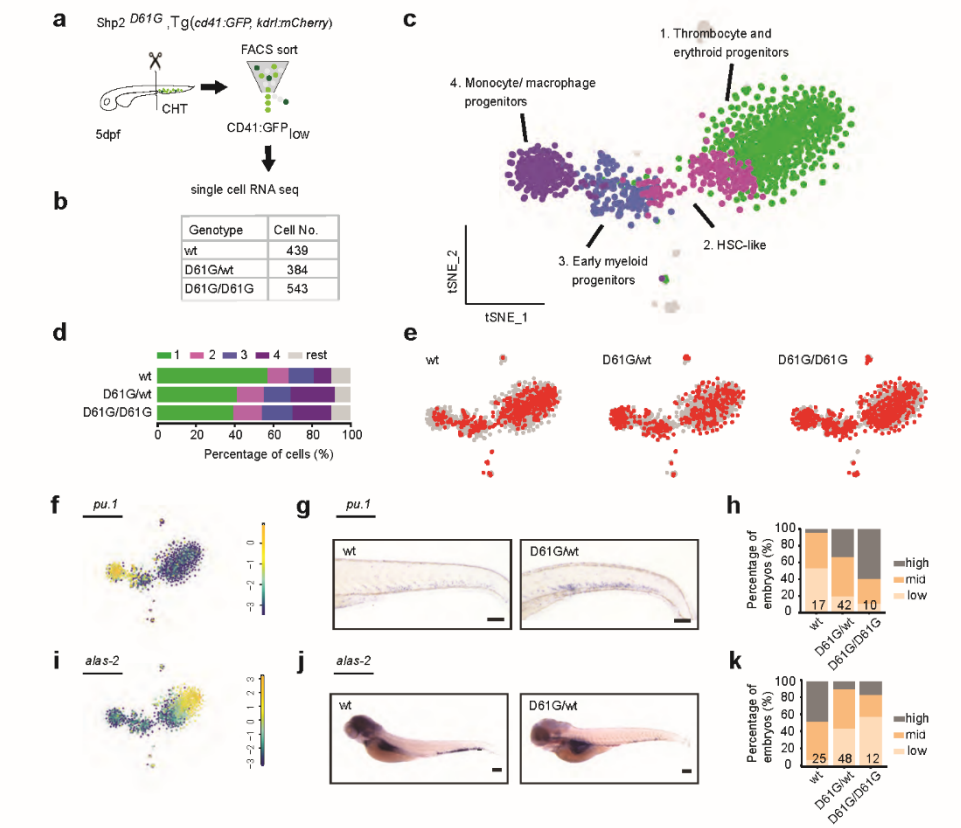

Figure 3. Single cell RNA sequencing of HSPCs reveals myeloid bias in Shp2^{D61G} embryos. a Schematic representation of the experimental procedure. At 5dpf, CHTs from Shp2^{wt}, Shp2$^{D61G/wt}$ and Shp2$^{D61G/D61G}$ embryos in Tg(*cd41*:*GFP, kdrl:mCherry-CAAX*) background were isolated. Cells were dissociated and separated by FACS, based on *cd41:GFP^{low}* expression, prior to single cell RNA sequencing, as described in the Materials and methods section. **b** Number of cells of distinct genotypes used in single cell RNA sequencing analysis. **c** Combined tSNE map generated using the cells of all three genotypes (Shp2^{wt}, Shp2$^{D61G/wt}$ and Shp2$^{D61G/D61G}$). Single cells from 4 major clusters are marked in violet, blue, pink and green and their identities based on marker gene expression are indicated. Minor clusters are marked in grey. **d** Barplots showing the percentage of cells of Shp2^{wt}, Shp2$^{D61G/wt}$ and Shp2$^{D61G/D61G}$ genotype in distinct clusters. **e** Cells of distinct genotypes Shp2^{wt}, Shp2$^{D61G/wt}$ and Shp2$^{D61G/D61G}$ are visualized in tSNE maps in red. **f** tSNE maps showing log2-transformed read-counts of *pu.1*. **g** Representative images of the WISH staining for *pu.1* expression in 5dpf Shp2^{wt} and Shp2^{D61G} zebrafish embryos. Scale bar,100μm. **h** Expression of the *pu.1* marker scored as low, mid and high. **i** tSNE maps showing log2-transformed read-counts of *alas-2*. **j** Representative images of the WISH staining for *alas-2* expression in the tail region of 5dpf Shp2^{wt} and Shp2^{D61G} zebrafish embryos. Scale bar, 100μm. **k** Expression of the *alas-2* marker scored as low, mid and high. **h,k** Number on bars: number of embryos.

Excessive proinflammatory response in monocyte/macrophage progenitors of Shp2^{D61G} HSPCs

We further analyzed the cluster of monocyte/macrophage progenitors, in which we observed an overrepresentation of mutant Shp2^{D61G} cells **(Fig. 4a)**. Functional annotation of the differentially expressed genes and the GO-term enrichment analysis revealed enhanced expression of proinflammatory genes in mutant Shp2^{D61G} cells (**Fig. 4a,b, Supplementary Table 1**). Interestingly, expression of inflammation-related genes, such as *gcsfa*, *gcsfb*, *il1b*, *irg1* and *nfkbiaa,* was

constrained to the cells of mutant Shp2^{D61G} genotype in the monocyte/macrophage progenitors cluster, whereas the monocyte marker *timp2a* was equally expressed by cells of distinct genotypes (**Fig. 4b)**. High expression of IL-1β was validated in mutant embryos *in vivo*, in which IL-1β-eGFP positive cells were more abundant in the CHT region of Shp2^{D61G} embryos than in wt embryos in the Tg(*il1b:eGFP*, *mpeg:mCherry*) transgenic background (**Fig. 4c)**. These results indicate that Shp2^{D61G} embryos display an inflammatory response at 5 dpf, which originates in the monocyte/macrophage progenitor cells.

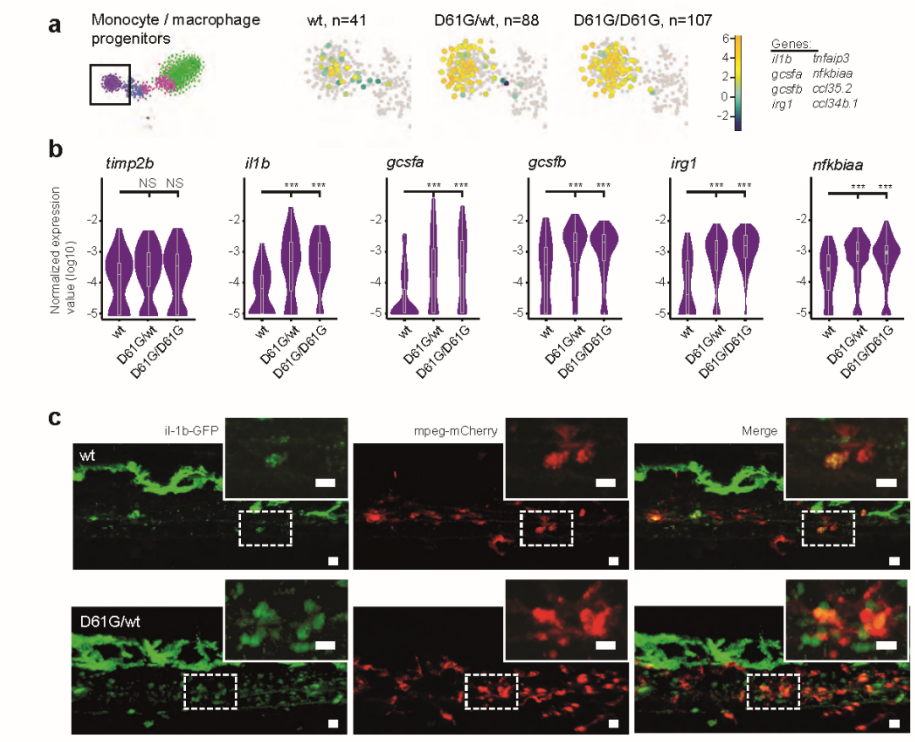

Figure 4. Inflammatory response in monocyte/ macrophage progenitors in Shp2^{D61G} embryos. **a** The monocyte/macrophage progenitors cluster (boxed on the tSNE map on left) was analyzed in detail. log2-transformed sum of read-counts of selected inflammation-related genes from the top 50 differentially expressed genes in the cells of the monocyte/macrophage progenitors cluster, with genotype and number of cells (n) indicated above. **b** Violin plots show the expression of specific genes in monocyte/macrophage progenitors of Shp2^{wt}, Shp2$^{D61G/wt}$ and Shp2$^{D61G/D61G}$ genotypes. NS, not significant, ***p < 0.001, t-test. **c** *In vivo* imaging of the CHT region of Shp2^{wt} and Shp2$^{D61G/wt}$ zebrafish embryos in Tg(*il1b:eGFP*, *mpeg:mCherry*) background at 5dpf. Representative images are shown. The dashed line boxed region of CHT is zoom-in in insert. Scale bar is 10μm.

PTPN11 **Somatic mutations induce inflammatory response genes in HSPCs of JMML patients.**

We hypothesized that activating mutations in Shp2 may trigger an inflammatory response in a similar way in sporadic JMML as we observed in syndromic JMML-like MPN. To investigate this, we performed transcriptomic analysis of the HSPCs compartments derived from bone marrows of sporadic JMML patients with activating mutations in SHP2 (n=5) and age-matched healthy donors (n=7). The SHP2 mutations in JMML HSPCs were distinct among patients (**Supplementary Table 2**). Overall, we identified 1478 differentially expressed genes (DEGs) in HSPCs from JMML patients, compared to the healthy donor HSPCs (**Fig. 5a**, **Supplementary Table 3**). The functional analysis of DEGs using gene set enrichment analysis (GSEA) was performed to systematically explore hallmark gene signatures specific for JMML HSPCs (**Fig. 5b, Supplementary Table 4**). Strikingly, altered expression of genes related to inflammation was the most prominent, such as genes involved in TNFa signaling via NFKb and inflammatory response genes, which were significantly enriched in JMML HSPCs (**Fig. 5b-d**). De-regulation of genes related to proliferation (G2M checkpoint, MYC targets and E2F targets) was evident in JMML HSPCs, suggesting their decreased quiescence (**Fig. 5b**).

We next studied whether the inflammatory-related gene signature overlaps between HSPCs from zebrafish NS/JMML-like MPN model and human JMML. GSEA revealed that human orthologs of the top 100 DEGs found in the zebrafish monocyte/macrophage progenitor cells were enriched significantly in patient JMML HSPCs (**Fig. 5e**). Some of the top overexpressed inflammation-associated genes in JMML patients, such as TNF and MARCKSL were also overexpressed in NS/JMML-like MPN mutant zebrafish embryos compared to the wt (**Fig. 5f,g**). 3D PCA analysis visualized that these zebrafish signature genes were able to clearly segregate HSPCs from JMML patients and healthy donors (**Fig. 5h**). These findings suggest that mutant, activated SHP2 triggers proinflammatory gene expression in HSPCs both in sporadic JMML patients and in our zebrafish model of syndromic JMML-like MPN in a similar manner, suggesting a common underlying, endogenously driven process.

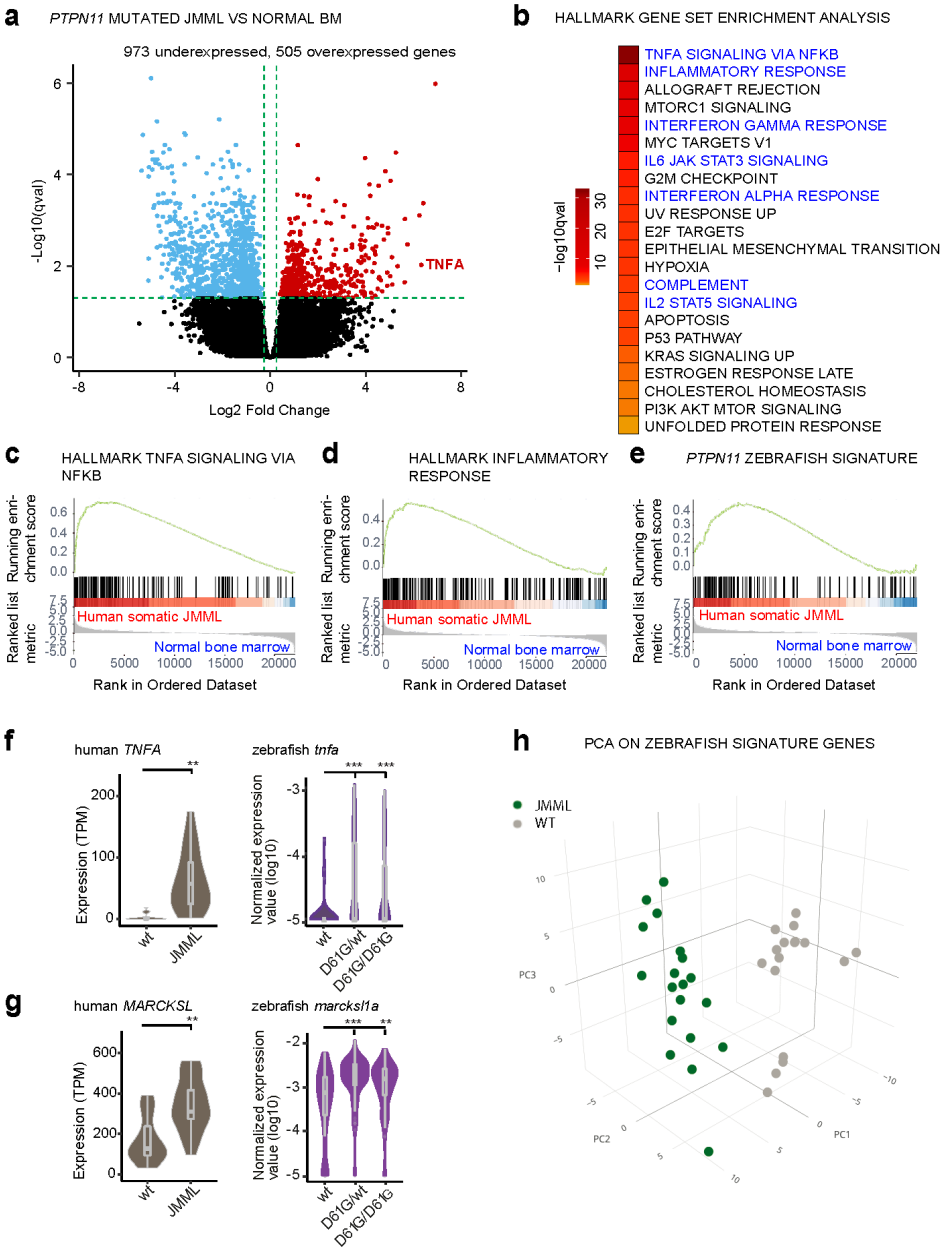

Figure 5. Similar molecular signatures in HSPCs from human JMML patients and zebrafish Shp2^{D61G} embryos. a Volcano plot of differentially expressed genes of HSPCs derived from bone marrow of JMML patients with *PTPN11* mutations (n=5) and healthy bone marrow (n=7). Underexpressed genes are marked in blue and overexpressed genes are marked in red. *TNFA* expression is highlighted. Green dashed lines indicate the significance level. **b** GSEA for the MSigDB's hallmark gene sets in HSPCs from JMML compared to normal human age-matched bone marrow. GSEA plots for TNFA_SIGNALING_VIA_NFKB (**c**), INFLAMMATORY RESPONSE (**d**), and the custom Zebrafish signature based on the top 100 human orthologous of genes upregulated in monocyte/macrophage progenitor cluster of zebrafish HSPCs (**e**). Violin plots show the expression of *TNFA* (**f**) and *MARCKSL* (**g**) in either human wt vs. JMML HSPCs, and zebrafish Shp2^{wt} vs. Shp2$^{D61G/wt}$ and Shp2$^{D61G/D61G}$ monocyte/macrophage HSPC progenitors. **p<0.01, ***p < 0.001, t-test. **h** PCA for the 100 genes included in the custom zebrafish signature. Green dots represent *PTPN11* mutated JMML, gray ones represent normal human age-matched bone marrow. PC1: 19% of the variance, PC2: 16% of the variance, PC3: 14% of the variance.

Inhibition of the proinflammatory response ameliorates the JMML-like MPN phenotype

Our results indicate that Shp2^{D61G} embryos displayed JMML-like MPN (**Fig. 2**). To investigate if pharmacological agents ameliorate the observed hematopoietic defects, Shp2^{D61G} embryos were exposed to inhibitors continuously from 2 to 5 dpf and subsequently *c-myb* and *l-plastin* markers were investigated by WISH (**Fig. 6a**). Inhibitors of the known Shp2-associated signaling pathways were used, targeting MEK (CI1040) or PI3K (LY294002) (Tajan et al., 2015). Both inhibitors led to a robust reduction in expansion of both HSPCs and myeloid lineage in mutant embryos (**Fig. 6b,c**), demonstrating that the NS-associated blood development defect in Shp2^{D61G} embryos was largely caused by overactivation of the RAS-MAPK and PI3K pathways as expected.

The HSPCs of Shp2^{D61G} embryos displayed a proinflammatory response (**Fig. 4**), similar to the inflammatory response in HSPCs from human patients (**Fig. 5**). To investigate the role of the inflammatory response in the blood defect, we assessed the effect of dexamethasone in Shp2^{D61G} embryos in parallel to the MEK- and PI3K inhibitors. Dexamethasone is an anti-inflammatory agent, which is known to suppress inflammatory response in the monocyte/macrophage lineage (Ehrchen et al., 2019). To our surprise, dexamethasone reduced *c-myb* and *l-plastin* expression to a similar extent as CI1040 and LY294002 (**Fig. 6b,c**), indicating a profound role for the inflammatory response in the pathogenesis of NS-associated blood defects. Taken together, we observed a proinflammatory phenotype of the macrophage/ monocyte lineage in Shp2^{D61G} mutant zebrafish, which is established early during HSPCs differentiation. Since an anti-inflammatory agent largely rescued the hematopoietic defects, we conclude that the inflammatory response in Shp2^{D61G} mutant zebrafish mediates the pathogenesis of the NS/JMML-like MPN blood phenotype.

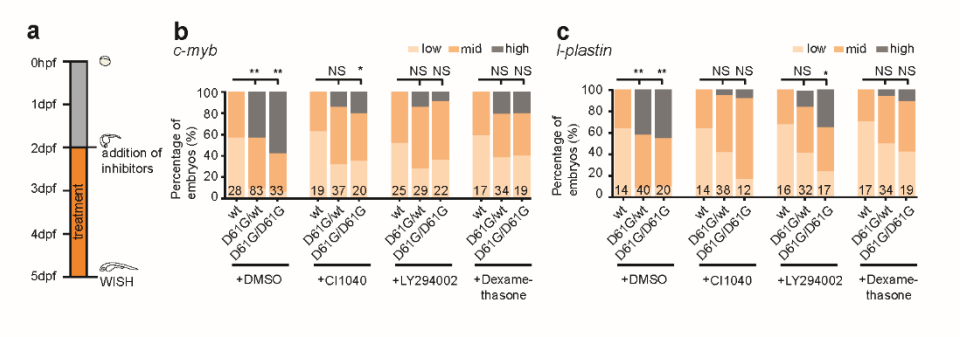

Figure 6. Anti-inflammatory treatment of zebrafish Shp2^{D61G} embryos ameliorates the JMML-like MPN phenotype. a Schematic overview of the treatments with MEK inhibitor CI1040, PI3K inhibitor LY294002 and anti-inflammatory corticosteroid dexamethasone. Embryos were continuously treated from 48hpf until 5dpf, when WISH was performed and expression of the *c-myb* (**b**) and *l-plastin* (**c**) marker was scored as low, mid and high. Measurements originate from at least three distinct experiments. Number on bars: number of embryos. NS, not significant; *p < 0.05, **p<0.01, ***p<0.001, Chi-squared test.

Discussion

To investigate the timing and pathophysiology of mutant SHP2-related myeloproliferative defects, we explored the transcriptomes of HSPCs with activating mutations in SHP2, derived from sporadic JMML patients and syndromic NS/JMML-like MPN zebrafish embryos, by bulk and single cell sequencing, respectively. Strikingly, proinflammatory gene expression was evident both in HSPCs from JMML patients and mutant zebrafish. Already early studies reported high levels of proinflammatory cytokines, such as IL-1β, TNF-α, GM-CSF, in JMML patients plasma (Bagby et al., 1988; Freedman et al., 1992). However, little is known about the cellular origin of the proinflammatory status, its pathophysiological role and therapeutic potential. The inflammatory response may be initiated in a cell autonomous way or in response to signals from the microenvironment. Dong et al. suggested that IL-1β is secreted by differentiated monocytes which get recruited upon secretion of the Chemokine, CCL3, by cells of the bone marrow microenvironment containing activating SHP2 mutations. However, the levels of CCL3 in the bone marrow of four NS patients varied (Dong et al., 2016). Furthermore, a microenvironment-driven inflammatory response would not explain high levels of cytokines in sporadic JMML, where niche cells are not mutated. On the other hand, recent reports indicate that JMML leukemia stem cells are heterogeneous but confined to the hematopoietic stem and progenitor cells (HSPCs) compartment, defining JMML HSPCs as the origin of the disease (Caye et al., 2019; Louka et al., 2021).

Here we identified HSPCs as the cells in which the proinflammatory status of the monocyte/macrophage lineage is initiated both in JMML and NS/JMML-like MPN. Hence, our data suggest that proinflammatory reprogramming of the monocyte/macrophage lineage might be endogenously driven at least in part, and detailed mechanisms remain to be elucidated in the future.

To our knowledge, the Shp2^{D61G} mutant zebrafish we developed is the first NS zebrafish model carrying an activating Shp2 mutation at its endogenous locus generated by CRISPR/Cas9-based knock-in technology. Strikingly, phenotypes developed by the Shp2^{D61G} zebrafish corroborate closely with the phenotypes displayed by human NS patients and the existing NS mouse models **(Fig. 1)**. Our model presents an exciting novel tool for deciphering pathogenesis mechanisms of NS with its complex traits and for finding novel therapies for this as yet poorly treatable condition.

NS children with D61G mutation have a higher predisposition to develop JMML(-like MPN), and comparably Shp2^{D61G} zebrafish embryos displayed typical JMML-like MPN characteristics, such as expansion of the myeloid lineage, increased sensitivity to gcsfa, mild anemia and thrombocytopenia **(Fig. 2)**. Furthermore, the observed blood defect was transplantable to secondary recipients and the disease originated in HSPCs, which displayed aberrant proliferation and apoptosis. Given the importance of fetal hematopoiesis during JMML(-like MPN) development, the zebrafish Shp2^{D61G} mutant represents a reliable and unique model for JMML-like MPN, which allows us to study hematopoietic defects caused by mutant Shp2 during the prenatal development for the first time. Our results suggest that the JMML-like MPN defect is initiated at the CHT, which is the counterpart of fetal liver in human. Here we observed expanded HSPCs, which displayed aberrant proliferation and apoptosis. We further characterized the transcriptomes of HSPCs specifically originating from the CHT, and studied their response to inhibitor treatments directly at the CHT. Striking similarities between the patient and zebrafish HSPCs transcriptomes indicate that the Shp2^{D61G} zebrafish model is an exciting preclinical model for *in vivo* drug screens at relevant developmental time points, in a high throughput manner.

The only effective treatment of JMML is allogeneic stem cell transplantation, which has a high relapse rate of 50%. Hence, there is a great need for other means of therapeutic intervention. The role of inflammation as one of the drivers in myeloid

leukemogenesis is emerging (Arranz et al., 2017; Craver et al., 2018). Here we demonstrate that dampening inflammation using the glucocorticoid dexamethasone, partially rescued the observed blood phenotype in Shp2^{D61G}, suggesting that the inflammatory response evoked in the cells of myeloid/macrophage lineage was an important driver of the NS/JMML-like blood defect and might be a potential drug target for both sporadic and syndromic JMML(-like MPN). To our surprise, targeting inflammation reversed the blood defect to a similar extent as the MAPK and PI3K pathway inhibitors, emphasizing not only the crucial role of inflammation during JMML pathogenesis, but also its strong therapeutic potential. Since anti-inflammatory therapies are non-invasive and widely available, targeting inflammation might represent a novel avenue for JMML treatment, either alone or in combination with other therapies.

In conclusion, we observed striking similarities in expression patterns of HSPCs from sporadic human JMML patients with an activating SHP2 mutation and HSPCs from an engineered zebrafish model with an activating NS-associated mutation in Shp2. Particularly genes associated with the inflammatory response were upregulated and strikingly, pharmacological inhibition of the inflammatory response ameliorated JMML-like MPN in the zebrafish model, suggesting this may be a first step for therapeutic intervention in human patients.

Materials and methods

Zebrafish husbandry

All procedures involving experimental animals were approved by the animal experiments committee of the Royal Netherlands Academy of Arts and Sciences (KNAW), Dierexperimenten commissie protocol HI18-0702, and performed under the local guidelines in compliance with national and European law. The following zebrafish lines were used in the study: Tübingen longfin (TL, wild type), Tg(*cd41:GFP, kdrl:mCherry-CAAX*) (Hogan et al., 2009; Lin et al., 2005), Tg*(mpx:GFP, mpeg:mCherry)* (Ellett et al., 2011; Renshaw et al., 2006), TgBAC(*il1b:eGFP*)sh445 (Ogryzko et al., 2019), *ptpn11b-/-* (Bonetti et al., 2014)*prkdc-/-* (Moore et al., 2016) and the novel Shp2^{D61G} zebrafish line. Raising and maintenance of zebrafish was performed according to (Aleström et al., 2020; Westerfield, 2000). When required, pigmentation of embryos was blocked by adding phenylthiourea (PTU) (Sigma Aldrich, St. Louis, MO, USA, Ref: P7629) at a concentration of 0.003% (v/v) to the E3 medium at 24hpf.

Patient material

All children's samples were obtained after parents had given their written informed consent. Experiments were approved by the institutional review board of the French Institute of Health and Medical Research (INSERM) (IORG0003254) in accordance with the Helsinki declaration. Healthy children bone marrows were obtained from intrafamilial BM transplantation donors and used with the approval of the Institutional Review Board of "Hôpitaux Universitaires Paris Nord Val-de-Seine," Paris 7 University, AP-HP), (IRB: 00006477), in accordance with the Helsinki declaration. HSPCs fractions were FACS sorted according to immunophenotypic signature as previously described (Caye et al., 2019), from PTPN11^{mut} JMML (n=5) and healthy children bone marrow (n=7). Age, sex, mutations and fractions available for each sample (Hematopoietic stem cells (HSCs), multipotent progenitors (MPPs), common myeloid progenitors (CMPs), granulocyte-macrophage progenitors (GMPs), and megakaryocyte-erythroid progenitors (MEPs)) are indicated in Supplementary Table 2.

Generation of the Shp2^{D61G} zebrafish line

The Shp2^{D61G} zebrafish line was generated using the previously described CRISPR/Cas9-based knock-in approach (Tessadori et al., 2018). The sgRNA

targeting exon 3 of the *ptpn11a* gene (5'- GGAGACTATTACGACCTGTA-3') was designed using the CHOP-CHOP database (http://chopchop.cbu.uib.no/), further processed according to the previously published guidelines (Gagnon et al., 2014) and finally transcribed using the Ambion MEGAscript T7 kit (TermoFisher Scientific, Waltham, MA, USA, Ref: AMB13345). The sgRNA, constant oligonucleotide and template oligonucleotide were all generated by Integrated DNA Technologies (IDT, Coralville, IA, USA) as standard desalted oligos and template oligonucleotide was further purified using the QIAquick Nucleotide Removal Kit (Qiagen, Hilden, Germany, Ref: 28304). The oligonucleotide used for the homology repair is 59 nucleotides long and besides the D61G mutation, contains three additional silent mutations in proximity of the PAM site. The sequence of template oligonucleotide is 5'-GAGTGGCAAACTTCTCTCCACCATATAAATCGTAATAGCCTCCTGTGTTTTGAATCTTA-3'. Tübingen longfin wt zebrafish embryos at the one-cell-stage were injected directly in the cell with 1 nl of the injection mixture containing 18.75 ng/ml of sgRNA, 37.5 ng/ml of template oligonucleotide and 3.6 mg/ml of Cas9 protein in 300 mM KCl. Cas9 protein was a gift from the Niels Geijsen laboratory at the Hubrecht Institute. The injected embryos were grown into the adulthood. F0 generation zebrafish were outcrossed with the wt zebrafish. DNA extracted from the 12 distinct 1dpf old F1 generation embryos was screened for the correct insertion of the template oligonucleotide. Screening was done by Sanger sequencing (Macrogen Europe B.V., Amsterdam, The Netherland) of the 225 bp long PCR product encompassing the genomic regions of the CRISPR target sites, which was generated using the forward 5'-TCATCTCCTCACTAGGCGAAAT-3' and reverse primer 5'- TATGTATGTGCTCACCTCTCGG-3'. The efficiency of the knock-in was 1.8% (1 founder zebrafish in 54 screened primary injected zebrafish). F1 generation was then established from the F0 founder. F1 generation adults were finclipped and sequenced for the presence of the mutation. All experiments were performed in zebrafish embryos and adults from the F3 and F4 generation. For most of the experiments, embryos were derived from an incross of Shp2$^{D61G/wt}$ animals. After the experimental procedure, embryos were lysed and genotyped by sequencing as described above. Western blotting was performed as previously described (Hale & den Hertog, 2017) using the Shp2 (Santa Cruz Biotechnology, Dallas, TX, USA, Ref: SC-280) and β-tubulin (Merck Millipore, Burlington, MA, USA Ref: CP06) antibodies.

Phenotyping of the NS traits

Body axis lengths were measured from the tip of the head to the end of the trunk in the bright-field images of laterally positioned embryos, larva and adults, which were anesthetized in 0.1% MS-222. Alcian blue (Sigma Aldrich, Ref: A5268) staining was performed as previously described (Paardekooper Overman et al., 2014), on PTU-treated 4dpf old embryos, which were anesthetized in 0.1% MS-222 and fixed in 4% PFA overnight. Embryos were positioned on their back in 70% glycerol in PBS and imaged with Leica M165 FC stereomicroscope (Leica Microsystems, Wetzlar, Germany. Analysis was performed in ImageJ. *In vivo* high-speed brightfield imaging of the embryonic hearts from PTU-treated embryos at 5dpf, which were anesthetized in 0.1% MS-222 and embedded in 0.3% UltraPure agarose (Thermo Fisher Scientific, Waltham, MA, USA) prepared in E3 medium containing 16 mg/ml MS-222. Measurements were performed at 28°C using a Leica DM IRBE inverted light microscope (Leica Microsystems) with a Hamamatsu C9300-221 high-speed CCD camera (Hamamatsu Photonics, Hamamatsu, Japan). Imaging was conducted at 150 frames per seconds (fps) using Hokawo 2.1 imaging software (Hamamatsu Photonics) for a period of 10 seconds (approximately 30 cardiac cycles). Heart rate measurements and contractility parameters were analysed using ImageJ. Volumes were analysed using ImageJ by drawing an ellipse on top of the ventricle at end-diastole and end-systole. Averages of three measurements per heart were determined. End diastolic and end systolic volume (EDV/ESV) were calculated by: (4/3)*(π)*(major axis/2)*((minor axis/2)^2). Stroke volume (SV) by: EDV-ESV. Ejection fraction (EF) by: (SV/EDV)*100. Cardiac output (CO) by: SV*Heart rate.

Whole mount *in situ* hybridization

PTU-treated embryos were anesthetized in 0.1% MS-222 (Sigma Aldrich, Ref: A5040) and fixed in 4% PFA for at least 12h at 4°C. *WISH* was performed as described in (Thisse et al., 1993)**.** Probes specific for *myl7*, *vhmc* and *ahmc* were described in (Bonetti et al., 2014). Probes specific for *c-myb*, *l-plastin*, *pu.1*, *gata1*, *ikaros*, *b-globin* and *alas-2* were described in (Choorapoikayil et al., 2014; Hu et al., 2014)**.** Subsequently, embryos were mounted in 70% glycerol in PBS and imaged with Leica M165 FC stereomicroscope (Leica Microsystems). Images were processed in ImageJ (U. S. National Institutes of Health, Bethesda, MD, USA). Abundance of the probe signal was scored as low, mild or high.

Inhibitors treatment

PTU-treated embryos were incubated with either 0.15μM of CI1040 (Sigma Aldrich, Ref: PZ0181), 4μM LY294002 (Sigma Aldrich, Ref: L9908) or 10μM of Dexamethasone (Sigma Aldrich, Ref: D4902) continuously from 24hpf until 5dpf. At 5dpf embryos were fixed and half of the embryos was processed for WISH using probe specific for *c-myb* and the other half using probe specific for *l-plastin*. Images were processed in ImageJ. Abundance of the probe signal was scored as low, mild or high.

Confocal microscopy

All confocal imaging was performed on a Leica SP8 confocal microscope (Leica Microsystems). Embryos were mounted in 0.3% agarose. Live embryos were anesthetized in MS-222. Whole embryos were imaged using a 10X objective and z-stack step size of $3\mu m$, while the CHT area with 20X objective and z-stack step size of $1\mu m$. The number of CD41-GFP^{low} cells was determined by imaging the CHT of the living 5dpf old embryos of the Shp2^{wt}, Shp2$^{D61G/wt}$ and Shp2$^{D61G/D61G}$ siblings in the Tg(*cd41:GFP, kdrl:mCherry-CAAX*) transgenic background, while the number of CD41-GFP^{high} cells was determined by imaging whole embryos, which were fixed for 2h in 4% PFA prior to imaging. To determine the number of mpx-GFP and mpeg-mCherry cells, whole live 5dpf old embryos of the Shp2^{wt}, Shp2$^{D61G/wt}$ and Shp2$^{D61G/D61G}$ line in the Tg*(mpx:GFP, mpeg:mCherry)* transgenic background were imaged. Imaris V9.3.1 (Bitplane, Zurich, Switzerland) was used to reconstruct 3D images and count individual GFP and/or mCherry positive cells.

Phosphorylated Histone 3 (pHis3) staining

PTU-treated 5dpf old Shp2^{D61G} embryos in the Tg(*cd41:GFP, kdrl:mCherry-CAAX*) transgenic background were fixed in 2% PFA overnight and stained as described in (Choorapoikayil et al., 2012). Primary pHis3 antibody (1:500 in blocking buffer, Abcam, Cambridge, UK, Ref: ab5176) and secondary GFP antibody (1:200 in blocking buffer, Aves Labs Inc. Tigard, OR, USA, GFP-1010) were used. Embryos were mounted in 0.3% agarose, their CHT was imaged using the SP8 confocal microscope and 3D images were subsequently reconstructed using Imaris.

Acridine orange staining

PTU-treated embryos at 5dpf were incubated in 5μg/ml of Acridine orange (Sigma Aldrich, Ref: A6014) in E3 medium, for 20 minutes at room temperature. They were then washed 5 times for 5 minutes in E3 medium, anesthetized in MS-222 and

mounted in 0.3% agarose. Whole embryos were imaged with SP8 confocal microscope and 3D images were reconstructed using Imaris.

Colony forming assay

The CD41-GFP^{low} cell population isolated from CHTs of Shp2^{wt}, Shp2$^{D61G/wt}$ embryos at 5dpf was FACS sorted. 250 µl of solution containing 2 500 cells, media prepared as described in (Svoboda et al., 2016), and 100 ng/ml of granulocyte colony stimulating factor a (Gscfa, gift from the Petr Bartunek lab, Institute of Molecular Genetics, Academy of Sciences of the Czech Republic v.v.i. Prague) was plated per well of a 96 well plate in a triplicate. Cells were grown in humidified incubators at 32°C, 5% CO_2. After 6 days colonies were imaged and counted using the EVOS microscope (Termo Fisher Scientific).

Transplantation experiments

Zebrafish kidney marrow transplantation were performed as previously described (Moore et al., 2016; Tang et al., 2014). In short, tissues were isolated from donor Shp2$^{D61G/wt}$ or wild type animals in the Tg(*mpx:GFP, mpeg:mCherry*) background following Tricaine (Western Chemical, Brussels, Belgium) overdose. Excised tissues from dissected fish are placed into 500 µl of 0.9x PBS + 5% FBS on a 10-cm Petri dish. Single-cell suspensions were obtained by maceration with a razor blade, followed by manual pipetting to disassociate cell clumps. Cells were filtered through a 40-µm Falcon cell strainer, centrifuged at 1,000 *g* for 10 min, and resuspended to the 2 x 10^7 cells/ml. 5-µl suspension containing 10^5 kidney marrow cells were injected into the peritoneal cavity of each recipient fish using a 26s Hamilton 80366 syringe. Cellular engraftment was assessed at 0, 7, 14, 28 dpt by epifluorescence microscopy.

Isolation of CD41-GFP^{low} cell population and single-cell RNA sequencing

From 24hpf onwards embryos were grown in PTU-containing medium. The CHTs of approximately 50 Shp2^{wt}, Shpt$^{D61G/wt}$ and Shp2$^{D61G/D61G}$ embryos in Tg(*cd41:GFP, kdrl:mCherry-CAAX*) transgenic background at 5dpf were dissected and collected in Leibovitz-medium (Thermo Fisher Scientific, Gibco, Ref: 11415049). After washing with PBS0 the CHTs were dissociated with TryplE (Thermo Fisher Scientific, Gibco, Ref: 12605036) for 45 minutes at 32°C. The resulting cell suspension was washed with PBS0, resuspended in PBS0 supplemented with 2mM EDTA, 2% FCS and 0.5µg/ml DAPI (Sigma Aldrich, Ref: D9542) and passed through a 40µm Falcon cell

strainer. DAPI staining was used to exclude dead cells. Cells with CD41-GFP^{low} positive signal were subjected to fluorescence-activated cell sorting (FACS) with an influx cytometer (BD Biosciences, San Jose, CA, USA). Single-cell RNA sequencing was performed according to an adapted version of the SORT-seq (Muraro et al., 2016) with adapted primers described in (Van Den Brink et al., 2017). In short, single cells were FACS sorted, as described above, on 384-well plates containing 384 primers and Mineral oil (Sigma Aldrich). After sorting, plates were snap-frozen on dry ice and stored at -80°C. For amplification cells were heat-lysed at 65°C followed by cDNA synthesis using the CEL-seq2 (Hashimshony et al., 2016) and robotic liquid handling platforms. After the second strand cDNA synthesis, the barcoded material was pooled into libraries of 384 cells and amplified using *in vitro* transcription. Following amplification, the rest of the CEL-seq2 protocol was followed for preparation of the amplified cDNA library, using TruSeq small RNA primers (Illumina, San Diego, CA, USA). The DNA library was paired-end sequenced on an Illumina Nextseq™ 500 (Illumina), high output, with a 1x75 bp Illumina kit (R1:26 cycles, index read: 6 cycles, R2:60 cycles).

Data analysis of single-cell RNA sequencing

During sequencing, Read1 was assigned 26 base pairs and was used for identification of the Ilumina library barcode, cell barcode and unique molecular identifier. Read2 was assigned 60 base pairs and used to map to the reference transcriptome of Zv9 Danio rerio. Data was demultiplexed as described in (Grün et al., 2014). Single cell transcriptomics analysis was done using the RaceID3 algorithm (Herman et al., 2018), following an adapted version of the RaceID manual (https://cran.r-project.org/web/packages/RaceID/vignettes/RaceID.html) using R-3.5.2. In total 768 cells per genotype were sequenced for the datasets. After removing cells with less than 1000 UMIs and only keeping genes that were detected with al least 3 UMIs in 1 cell, 439 wt, 384 D61G/wt and 543 D61G/D61G cells were left for further analysis. Batch effects observed for plates which were prepared on different days was removed using the scran function. 4 major clusters and 5 minor clusters were identified. The minor clusters contained 130 cells in total and were excluded from further analysis for statistical reasons. Differential gene expression analysis was done as described in (Muraro et al., 2016) with an adapted version of the DESseq2 (Love et al., 2014). GO term enrichment analysis for differentially

expressed genes of each major cluster was performed using the DAVID Bioinformatics Resources 6.8 (https://david.ncifcrf.gov/).

RNA sequencing and differential gene expression analysis of the patient material

Libraries were prepared with TruSeq® Stranded Total RNASample preparation kit (Illumina) according to supplier's recommendations. Briefly, the ribosomal RNA fraction was removed from 1µg of total RNA using the Ribo-Zero™ Gold Kit (Illumina). Fragmentation was then achieved using divalent cations under elevated temperature to obtain approximately 300bp pieces. Double strand cDNA synthesis was performed using reverse transcriptase and random primers, Illumina adapters were ligated and cDNA library was PCR amplified for sequencing. Paired-end 75b sequencing was then carried out on a HiSeq4000 (Illumina). Quality of reads was assessed for each sample using FastQC (http://www.bioinformatics.babraham.ac.uk/projects/fastqc/). A subset of 500,000 reads from each Fastq file was aligned to the reference human genome hg19/GRCh37 with tophat2 to determine insert sizes with Picard. Full Fastq files were aligned to the reference human genome hg19/GRCh37 with tophat2 (-p 24 -r 150 -g 2 --library-type fr-firststrand) (Kim et al., 2013). We removed reads mapping to multiple locations. STAR was used to obtain the number of reads associated with each gene in the Gencode v26lift37 annotation (restricted to protein-coding genes, antisense, and lincRNAs). Raw counts for each sample were imported into R statistical software using the Bioconductor DESeq2 package. Extracted count matrix was normalized for library size and coding length of genes to compute TPM expression levels. Differential gene expression analysis was performed using the Bioconductor limma package and the voom transformation. To improve the statistical power of the analysis, only genes expressed in at least one sample (TPM >0.3) were considered. A qval threshold of < 0.05 and a minimum fold change of 1.2 were used to define differentially expressed genes. Due to the imbalance between male and female samples, sex differences were adjusted with the function model.matrix from the stats package. RNAseq data analysis was performed with Galileo® v1.4.4, an interactive R shiny application. Representations of the gene expression levels were performed with the library ggplot2 and R 4.0.2.

Pathway enrichment analysis (GSEA) and Principal component analysis (PCA)

Gene set enrichment analysis was performed by clusterProfiler::GSEA function using the fgsea algorithm. Gene list from the differential analysis was ordered by decreasing

log2 (fold change). Hallmark classes Gene sets from the MSigDB v7.2 database were selected keeping only gene sets defined by 10-500 genes. The p-values were adjusted by the Benjamini-Hochberg (FDR) procedure. The custom zebrafish signature was built from the human orthologous genes of the 100 most overexpressed zebrafish genes based on the log2 (Fold Change) derived from the monocyte/macrophage progenitor cluster of the zebrafish HSPCs single cell sequencing dataset. The Bioconductor edgeR package was used to import raw counts into R, and compute normalized log2 CPM (counts per millions of mapped reads) using the TMM (weighted trimmed mean of M-values) as normalization procedure. The normalized expression matrix from the 100 most overexpressed genes (based on log2FC in the zebrafish dataset) was used to classify the samples according to their gene expression patterns using principal component analysis (PCA). PCA was performed by FactoMineR::PCA function with “ncp = 10, scale.unit = FALSE” parameters.

Statistical analysis

Data was plotted in GraphPad Prism 7.05 (GraphPad Software Inc., San Diego, CA, USA), except for the violin plots of gene expression, which were plotted in R using ggplot2(Wickham, 2009). Statistical difference analysis was performed using the one-way ANOVA supplemented by Tukey’s HSD test in GraphPad Prism 7.05, except for the gene expression differences in single cell RNA sequencing data, where T-test was performed in Rstudio 1.1.463 (Rstudio, Boston, MA, USA), and the treatment WISH experiments, where Chi-squared test was performed in GraphPad Prism 7.05. Significant difference was considered when $p<0.05$ (*$p<0.05$, **$p<0.01$, ***$p<0.001$, NS=non significant).

Author Contributions

MS Conceptualization, Methodology, Formal analysis, Investigation, Data Curation, Writing - Original Draft, Visualization, **SBF** Investigation, Formal analysis, Data Curation, Methodology, Writing - Review & Editing, **FP** Investigation, Formal Analysis, Methodology, Writing - Review Editing, **CY, QY** Investigation- performed transplantation experiments, Data Curation, Formal analysis, Methodology, Writing - Review & Editing**, MS** Investigation, Formal Analysis, Methodology**, SMK** Investigation- provided assistance with heart function analysis, Methodology, Resources, Writing - Review & Editing**, JB** Conceptualization, Supervision, Writing - Review & Editing**, DML** Conceptualization, Supervision, Writing - Review & Editing**, HC** Conceptualization, Supervision, Writing - Review & Editing, **JDH** Conceptualization, Supervision, Funding acquisition, Project administration, Writing - Original Draft

Acknowledgements

We thank the laboratory of Niels Geijsen (Hubrecht Institute) for providing us with Cas9 protein, Petr Bartunek and Olga Machanova (Institute of Molecular Genetics, Academy of Sciences of the Czech Republic v.v.i. Prague) and Geert Wiegertjes (University Wageningen) for cytokines and carp serum, Stefan van der Elst for assistance with FACS sorting, Hubrecht Institute animal caretakers for animal support and Single Cell Discoveries and Chloé Baron for support with single cell RNA sequencing. This work was supported by E-Rare grant NSEuroNet (JdH and HC), EJPRD grant NSEuroNet (JdH and HC), NIH grants R01CA211734 (D.M.L) and R24OD016761 (D.M.L), the MGH Research Scholar Award (D.M.L.) and Alex Lemonade Stand Foundation (C.Y.).

Competing Interests:

The authors declare no competing interests.

References

Aleström, P., D'Angelo, L., Midtlyng, P. J., Schorderet, D. F., Schulte-Merker, S., Sohm, F., & Warner, S. (2020). Zebrafish: Housing and husbandry recommendations. *Laboratory Animals*, *54*(3), 213–224. https://doi.org/10.1177/0023677219869037

Araki, T., Chan, G., Newbigging, S., Morikawa, L., Bronson, R., & Neel, B. G. (2009). Noonan syndrome cardiac defects are caused by PTPN11 acting in endocardium to enhance endocardial-mesenchymal transformation. *Proceedings of the National Academy of Sciences of the United States of America*, *106*(12), 4736–4741. https://doi.org/10.1073/pnas.0810053106

Araki, T., Mohi, M. G., Ismat, F. A., Bronson, R. T., Williams, I. R., Kutok, J. L., Yang, W., Pao, L. I., Gilliland, D. G., Epstein, J. A., & Neel, B. G. (2004). Mouse model of Noonan syndrome reveals cell type- and gene dosage-dependent effects of Ptpn11 mutation. *Nature Medicine*, *10*(8), 849–857. https://doi.org/10.1038/nm1084

Arranz, L., Arriero, M. del M., & Villatoro, A. (2017). Interleukin-1β as emerging therapeutic target in hematological malignancies and potentially in their complications. In *Blood Reviews* (Vol. 31, Issue 5, pp. 306–317). Churchill Livingstone. https://doi.org/10.1016/j.blre.2017.05.001

Bagby, G. C., Dinarello, C. A., Neerhout, R. C., Ridgway, D., & McCall, E. (1988). Interleukin 1-dependent paracrine granulopoiesis in chronic granulocytic leukemia of the juvenile type. *Journal of Clinical Investigation*, *82*(4), 1430–1436. https://doi.org/10.1172/JCI113748

Behnert, A., Meyer, J., Parsa, J.-Y., Hechmer, A., Loh, M. L., Olshen, A., Smith, A. J. de, & Stieglitz, E. (2021). Exploring the genetic and epigenetic origins of juvenile myelomonocytic leukemia using newborn screening samples. *Leukemia 2021*, 1–4. https://doi.org/10.1038/s41375-021-01331-0

Bonetti, M., Rodriguez-Martinez, V., Overman, J. P., Overvoorde, J., Van Eekelen, M., Jopling, C., & Den Hertog, J. (2014). Distinct and overlapping functions of ptpn11 genes in zebrafish development. *PLoS ONE*, *9*(4), e94884. https://doi.org/10.1371/journal.pone.0094884

Caye, A., Rouault-Pierre, K., Strullu, M., Lainey, E., Abarrategi, A., Fenneteau, O., Arfeuille, C., Osman, J., Cassinat, B., Pereira, S., Anjos-Afonso, F., Currie, E.,

692 Ariza-McNaughton, L., Barlogis, V., Dalle, J. H., Baruchel, A., Chomienne, C.,
693 Cavé, H., & Bonnet, D. (2019). Despite mutation acquisition in hematopoietic
694 stem cells, JMML-propagating cells are not always restricted to this
695 compartment. *Leukemia*, 1–11. https://doi.org/10.1038/s41375-019-0662-y
696 Caye, A., Strullu, M., Guidez, F., Cassinat, B., Gazal, S., Fenneteau, O., Lainey, E.,
697 Nouri, K., Nakhaei-Rad, S., Dvorsky, R., Lachenaud, J., Pereira, S., Vivent, J.,
698 Verger, E., Vidaud, D., Galambrun, C., Picard, C., Petit, A., Contet, A., … Cavé,
699 H. (2015). Juvenile myelomonocytic leukemia displays mutations in components
700 of the RAS pathway and the PRC2 network. *Nature Genetics 2015 47:11*,
701 *47*(11), 1334–1340. https://doi.org/10.1038/ng.3420
702 Chan, G., Kalaitzidis, D., Usenko, T., Kutok, J. L., Yang, W., Mohi, M. G., & Neel, B.
703 G. (2009). Leukemogenic Ptpn11 causes fatal myeloproliferative disorder via
704 cell-autonomous effects on multiple stages of hematopoiesis. *Blood*, *113*(18),
705 4414–4424. https://doi.org/10.1182/BLOOD-2008-10-182626
706 Choorapoikayil, S., Kers, R., Herbomel, P., Kissa, K., & den Hertog, J. (2014).
707 Pivotal role of Pten in the balance between proliferation and differentiation of
708 hematopoietic stem cells in zebrafish. *Blood*, *123*(2), 184–190.
709 https://doi.org/10.1182/BLOOD-2013-05-501544
710 Choorapoikayil, S., Kuiper, R. V, de Bruin, A., & den Hertog, J. (2012).
711 Haploinsufficiency of the genes encoding the tumor suppressor Pten
712 predisposes zebrafish to hemangiosarcoma. *Disease Models & Mechanisms*,
713 *5*(2), 241–247. https://doi.org/10.1242/dmm.008326
714 Craver, B. M., El Alaoui, K., Scherber, R. M., & Fleischman, A. G. (2018). The critical
715 role of inflammation in the pathogenesis and progression of myeloid
716 malignancies. In *Cancers* (Vol. 10, Issue 4). MDPI AG.
717 https://doi.org/10.3390/cancers10040104
718 de Pater, E., & Trompouki, E. (2018). Bloody Zebrafish: Novel Methods in Normal
719 and Malignant Hematopoiesis. *Frontiers in Cell and Developmental Biology*, *6*,
720 124. https://doi.org/10.3389/fcell.2018.00124
721 Dong, L., Yu, W. M., Zheng, H., Loh, M. L., Bunting, S. T., Pauly, M., Huang, G.,
722 Zhou, M., Broxmeyer, H. E., Scadden, D. T., & Qu, C. K. (2016).
723 Leukaemogenic effects of Ptpn11 activating mutations in the stem cell
724 microenvironment. *Nature*, *539*(7628), 304–308.
725 https://doi.org/10.1038/nature20131

726 Ehrchen, J. M., Roth, J., & Barczyk-Kahlert, K. (2019). More Than Suppression:
727 Glucocorticoid Action on Monocytes and Macrophages. *Frontiers in*
728 *Immunology*, *0*(AUG), 2028. https://doi.org/10.3389/FIMMU.2019.02028
729 Ellett, F., Pase, L., Hayman, J. W., Andrianopoulos, A., & Lieschke, G. J. (2011).
730 mpeg1 promoter transgenes direct macrophage-lineage expression in zebrafish.
731 *Blood*, *117*(4), e49. https://doi.org/10.1182/blood-2010-10-314120
732 Freedman, M. H., Cohen, A., Grunberger, T., Bunin, N., Luddy, R. E., Saunders, E.
733 F., Shahidi, N., Lau, A., & Estrov, Z. (1992). Central role of tumour necrosis
734 factor, GM-CSF, and interleukin 1 in the pathogenesis of juvenile chronic
735 myelogenous leukaemia. *British Journal of Haematology*, *80*(1), 40–48.
736 https://doi.org/10.1111/j.1365-2141.1992.tb06398.x
737 Gagnon, J. A., Valen, E., Thyme, S. B., Huang, P., Akhmetova, L., Ahkmetova, L.,
738 Pauli, A., Montague, T. G., Zimmerman, S., Richter, C., & Schier, A. F. (2014).
739 Efficient mutagenesis by Cas9 protein-mediated oligonucleotide insertion and
740 large-scale assessment of single-guide RNAs. *PloS One*, *9*(5), e98186.
741 https://doi.org/10.1371/journal.pone.0098186
742 Gore, A. V., Pillay, L. M., Venero Galanternik, M., & Weinstein, B. M. (2018). The
743 zebrafish: A fintastic model for hematopoietic development and disease. *Wiley*
744 *Interdisciplinary Reviews: Developmental Biology*, *7*(3), e312.
745 https://doi.org/10.1002/wdev.312
746 Grün, D., Kester, L., & Van Oudenaarden, A. (2014). Validation of noise models for
747 single-cell transcriptomics. *Nature Methods*, *11*(6), 637–640.
748 https://doi.org/10.1038/nmeth.2930
749 Hale, A. J., & den Hertog, J. (2017). Shp2–Mitogen-Activated Protein Kinase
750 Signaling Drives Proliferation during Zebrafish Embryo Caudal Fin Fold
751 Regeneration. *Molecular and Cellular Biology*, *38*(4).
752 https://doi.org/10.1128/mcb.00515-17
753 Hashimshony, T., Senderovich, N., Avital, G., Klochendler, A., de Leeuw, Y., Anavy,
754 L., Gennert, D., Li, S., Livak, K. J., Rozenblatt-Rosen, O., Dor, Y., Regev, A., &
755 Yanai, I. (2016). CEL-Seq2: Sensitive highly-multiplexed single-cell RNA-Seq.
756 *Genome Biology*, *17*(1), 77. https://doi.org/10.1186/s13059-016-0938-8
757 Herman, J. S., Sagar, & Grün, D. (2018). FateID infers cell fate bias in multipotent
758 progenitors from single-cell RNA-seq data. *Nature Methods*, *15*(5), 379–386.
759 https://doi.org/10.1038/nmeth.4662

760 Hogan, B. M., Bos, F. L., Bussmann, J., Witte, M., Chi, N. C., Duckers, H. J., &
761 Schulte-Merker, S. (2009). Ccbe1 is required for embryonic lymphangiogenesis
762 and venous sprouting. *Nature Genetics*, *41*(4), 396–398.
763 https://doi.org/10.1038/ng.321
764 Hu, B., Zhang, W., Feng, X., Ji, W., Xie, X., & Xiao, W. (2014). Zebrafish eaf1
765 suppresses foxo3b expression to modulate transcriptional activity of gata1 and
766 spi1 in primitive hematopoiesis. *Developmental Biology*, *388*(1), 81–93.
767 https://doi.org/10.1016/j.ydbio.2014.01.005
768 Jopling, C., Van Geemen, D., & Den Hertog, J. (2007). Shp2 knockdown and
769 noonan/LEOPARD mutant Shp2-induced gastrulation defects. *PLoS Genetics*,
770 *3*(12), e225. https://doi.org/10.1371/journal.pgen.0030225
771 Kratz, C. P., Niemeyer, C. M., Castleberry, R. P., Cetin, M., Bergsträsser, E.,
772 Emanuel, P. D., Hasle, H., Kardos, G., Klein, C., Kojima, S., Stary, J., Trebo, M.,
773 Zecca, M., Gelb, B. D., Tartaglia, M., & Loh, M. L. (2005). The mutational
774 spectrum of PTPN11 in juvenile myelomonocytic leukemia and Noonan
775 syndrome/myeloproliferative disease. *Blood*, *106*(6), 2183–2185.
776 https://doi.org/10.1182/blood-2005-02-0531
777 Lin, H. F., Traver, D., Zhu, H., Dooley, K., Paw, B. H., Zon, L. I., & Handin, R. I.
778 (2005). Analysis of thrombocyte development in CD41-GFP transgenic
779 zebrafish. *Blood*, *106*(12), 3803–3810. https://doi.org/10.1182/blood-2005-01-
780 0179
781 Louka, E., Povinelli, B., Rodriguez-Meira, A., Buck, G., Wen, W. X., Wang, G.,
782 Sousos, N., Ashley, N., Hamblin, A., Booth, C. A. G., Roy, A., Elliott, N.,
783 Iskander, D., De La Fuente, J., Fordham, N., O'Byrne, S., Inglott, S., Norfo, R.,
784 Salio, M., … Mead, A. J. (2021). Heterogeneous disease-propagating stem cells
785 in juvenile myelomonocytic leukemia. *Journal of Experimental Medicine*, *218*(2).
786 https://doi.org/10.1084/JEM.20180853
787 Love, M. I., Huber, W., & Anders, S. (2014). Moderated estimation of fold change
788 and dispersion for RNA-seq data with DESeq2. *Genome Biology*, *15*(12), 550.
789 https://doi.org/10.1186/s13059-014-0550-8
790 Moore, J. C., Tang, Q., Yordán, N. T., Moore, F. E., Garcia, E. G., Lobbardi, R.,
791 Ramakrishnan, A., Marvin, D. L., Anselmo, A., Sadreyev, R. I., & Langenau, D.
792 M. (2016). Single-cell imaging of normal and malignant cell engraftment into
793 optically clear prkdc-null scid zebrafish. *Journal of Experimental Medicine*,

213(12), 2575–2589. https://doi.org/10.1084/jem.20160378

Mulero-Navarro, S., Sevilla, A., Roman, A. C., Lee, D.-F., D'Souza, S. L., Pardo, S., Riess, I., Su, J., Cohen, N., Schaniel, C., Rodriguez, N. A., Baccarini, A., Brown, B. D., Cavé, H., Caye, A., Strullu, M., Yalcin, S., Park, C. Y., Dhandapany, P. S., … Gelb, B. D. (2015). Myeloid Dysregulation in a Human Induced Pluripotent Stem Cell Model of PTPN11 -Associated Juvenile Myelomonocytic Leukemia. *Cell Reports*, *13*(3), 504–515. https://doi.org/10.1016/j.celrep.2015.09.019

Muraro, M. J., Dharmadhikari, G., Grün, D., Groen, N., Dielen, T., Jansen, E., van Gurp, L., Engelse, M. A., Carlotti, F., de Koning, E. J. P., & van Oudenaarden, A. (2016). A Single-Cell Transcriptome Atlas of the Human Pancreas. *Cell Systems*, *3*(4), 385-394.e3. https://doi.org/10.1016/j.cels.2016.09.002

Niihori, T., Nagai, K., Fujita, A., Ohashi, H., Okamoto, N., Okada, S., Harada, A., Kihara, H., Arbogast, T., Funayama, R., Shirota, M., Nakayama, K., Abe, T., Inoue, S. ichi, Tsai, I. C., Matsumoto, N., Davis, E. E., Katsanis, N., & Aoki, Y. (2019). Germline-Activating RRAS2 Mutations Cause Noonan Syndrome. *American Journal of Human Genetics*, *104*(6), 1233–1240. https://doi.org/10.1016/j.ajhg.2019.04.014

Ogryzko, N. V., Lewis, A., Wilson, H. L., Meijer, A. H., Renshaw, S. A., & Elks, P. M. (2019). Hif-1α–Induced Expression of Il-1β Protects against Mycobacterial Infection in Zebrafish. *The Journal of Immunology*, *202*(2), 494–502. https://doi.org/10.4049/JIMMUNOL.1801139

Paardekooper Overman, J., Yi, J.-S., Bonetti, M., Soulsby, M., Preisinger, C., Stokes, M. P., Hui, L., Silva, J. C., Overvoorde, J., Giansanti, P., Heck, A. J. R., Kontaridis, M. I., Den Hertog, J., & Bennett, A. M. (2014). PZR Coordinates Shp2 Noonan and LEOPARD Syndrome Signaling in Zebrafish and Mice. *Molecular and Cellular Biology*, *34*(15), 2874–2889. https://doi.org/10.1128/MCB.00135-14

Rauen, K. A. (2013). The RASopathies. *Annu. Rev. Genomics Hum. Genet*, *14*, 355–369. https://doi.org/10.1146/annurev-genom-091212-153523

Renshaw, S. A., Loynes, C. A., Trushell, D. M. I., Elworthy, S., Ingham, P. W., & Whyte, M. K. B. (2006). A transgenic zebrafish model of neutrophilic inflammation. *Blood*, *108*(13), 3976–3978. https://doi.org/10.1182/blood-2006-05-024075

Runtuwene, V., van Eekelen, M., Overvoorde, J., Rehmann, H., Yntema, H. G.,

828 Nillesen, W. M., van Haeringen, A., van der Burgt, I., Burgering, B., & den
829 Hertog, J. (2011). Noonan syndrome gain-of-function mutations in NRAS cause
830 zebrafish gastrulation defects. *Disease Models & Mechanisms*, *4*(3), 393–399.
831 https://doi.org/10.1242/dmm.007112
832 Strullu, M., Caye, A., Lachenaud, J., Cassinat, B., Gazal, S., Fenneteau, O.,
833 Pouvreau, N., Pereira, S., Baumann, C., Contet, A., Sirvent, N., Méchinaud, F.,
834 Guellec, I., Adjaoud, D., Paillard, C., Alberti, C., Zenker, M., Chomienne, C.,
835 Bertrand, Y., … Cavé, H. (2014). Juvenile myelomonocytic leukaemia and
836 Noonan syndrome. *Journal of Medical Genetics*, *51*(10), 689–697.
837 https://doi.org/10.1136/jmedgenet-2014-102611
838 Svoboda, O., Stachura, D. L., MacHonova, O., Zon, L. I., Traver, D., & Bartunek, P.
839 (2016). Ex vivo tools for the clonal analysis of zebrafish hematopoiesis. *Nature*
840 *Protocols*, *11*(5), 1007–1020. https://doi.org/10.1038/nprot.2016.053
841 Tajan, M., de Rocca Serra, A., Valet, P., Edouard, T., & Yart, A. (2015). SHP2 sails
842 from physiology to pathology. In *European Journal of Medical Genetics* (Vol. 58,
843 Issue 10, pp. 509–525). https://doi.org/10.1016/j.ejmg.2015.08.005
844 Tajan, M., Paccoud, R., Branka, S., Edouard, T., & Yart, A. (2018). The RASopathy
845 Family: Consequences of Germline Activation of the RAS/MAPK Pathway.
846 *Endocrine Reviews*, *39*(5), 676–700. https://doi.org/10.1210/er.2017-00232
847 Tang, Q., Abdelfattah, N. S., Blackburn, J. S., Moore, J. C., Martinez, S. A., Moore,
848 F. E., Lobbardi, R., Tenente, I. M., Ignatius, M. S., Berman, J. N., Liwski, R. S.,
849 Houvras, Y., & Langenau, D. M. (2014). Optimized cell transplantation using
850 adult rag2 mutant zebrafsh. *Nature Methods*, *11*(8), 821–824.
851 https://doi.org/10.1038/nmeth.3031
852 Tarnawsky, S. P., Yoshimoto, M., Deng, L., Chan, R. J., & Yoder, M. C. (2017). Yolk
853 Sac Erythromyeloid Progenitors Expressing Gain Of Function PTPN11 Have
854 Functional Features Of JMML But Are Not Sufficient To Cause Disease In Mice.
855 *Developmental Dynamics : An Official Publication of the American Association of*
856 *Anatomists*, *246*(12), 1001. https://doi.org/10.1002/DVDY.24598
857 Tarnawsky, S. P., Yu, W.-M., Qu, C.-K., Chan, R. J., & Yoder, M. C. (2018).
858 Hematopoietic-restricted Ptpn11E76K reveals indolent MPN progression in
859 mice. *Oncotarget*, *9*(31), 21831. https://doi.org/10.18632/ONCOTARGET.25073
860 Tartaglia, M., Mehler, E. L., Goldberg, R., Zampino, G., Brunner, H. G., Kremer, H.,
861 Van der Burgt, I., Crosby, A. H., Ion, A., Jeffery, S., Kalidas, K., Patton, M. A.,

Kucherlapati, R. S., & Gelb, B. D. (2001). Mutations in PTPN11, encoding the protein tyrosine phosphatase SHP-2, cause Noonan syndrome. *Nature Genetics*, *29*(4), 465–468. https://doi.org/10.1038/ng772

Tartaglia, M., Niemeyer, C. M., Fragale, A., Song, X., Buechner, J., Jung, A., Hählen, K., Hasle, H., Licht, J. D., & Gelb, B. D. (2003). Somatic mutations in PTPN11 in juvenile myelomonocytic leukemia, myelodysplastic syndromes and acute myeloid leukemia. *Nature Genetics*, *34*(2), 148–150. https://doi.org/10.1038/ng1156

Tessadori, F., Roessler, H. I., Savelberg, S. M. C., Chocron, S., Kamel, S. M., Duran, K. J., Van Haelst, M. M., Van Haaften, G., & Bakkers, J. (2018). Effective CRISPR/Cas9-based nucleotide editing in zebrafish to model human genetic cardiovascular disorders. *Disease Models and Mechanisms*, *11*(10). https://doi.org/10.1242/dmm.035469

Tessadori, F., van Weerd, J. H., Burkhard, S. B., Verkerk, A. O., de Pater, E., Boukens, B. J., Vink, A., Christoffels, V. M., & Bakkers, J. (2012). Identification and Functional Characterization of Cardiac Pacemaker Cells in Zebrafish. *PLoS ONE*, *7*(10), e47644. https://doi.org/10.1371/journal.pone.0047644

Thisse, C., Thisse, B., Schilling, T. F., & Postlethwait, J. H. (1993). Structure of the zebrafish snail1 gene and its expression in wild-type, spadetail and no tail mutant embryos. *Development*, *119*(4).

Van Den Brink, S. C., Sage, F., Vértesy, Á., Spanjaard, B., Peterson-Maduro, J., Baron, C. S., Robin, C., & Van Oudenaarden, A. (2017). Single-cell sequencing reveals dissociation-induced gene expression in tissue subpopulations. In *Nature Methods* (Vol. 14, Issue 10, pp. 935–936). Nature Publishing Group. https://doi.org/10.1038/nmeth.4437

Westerfield, M. (2000). *The Zebrafish Book: A Guide for the Laboratory Use of Zebrafish (Danio Rerio)* (4th ed.). University of Oregon Press.

Wickham, H. (2009). *ggplot2: Elegant Graphics for Data Analysis*. Springer International Publishing. https://ggplot2.tidyverse.org.

Xu, D., Liu, X., Yu, W. M., Meyerson, H. J., Guo, C., Gerson, S. L., & Qu, C. K. (2011). Non-lineage/stage-restricted effects of a gain-of-function mutation in tyrosine phosphatase Ptpn11 (Shp2) on malignant transformation of hematopoietic cells. *Journal of Experimental Medicine*, *208*(10), 1977–1988. https://doi.org/10.1084/jem.20110450

896